Chemical Science

EDGE ARTICLE

View Article Online
View Journal | View Issue

Check for updates

Cite this: *Chem. Sci.*, 2019, **10**, 2893

All publication charges for this article have been paid for by the Royal Society of Chemistry

Influence of intramolecular secondary sphere hydrogen-bonding interactions on cytochrome *c* oxidase inspired low-spin heme–peroxo–copper complexes†

Melanie A. Ehudin, ‡[a] Andrew W. Schaefer, ‡[b] Suzanne M. Adam,[a] David A. Quist, [a] Daniel E. Diaz,[a] Joel A. Tang,[a] Edward I. Solomon *[b] and Kenneth D. Karlin *[a]

Dioxygen reduction by heme–copper oxidases is a critical biochemical process, wherein hydrogen bonding is hypothesized to participate in the critical step involving the active-site reductive cleavage of the O–O bond. Sixteen novel synthetic heme–(μ-O_2^{2-})–Cu(^{X}TMPA) complexes, whose design is inspired by the cytochrome *c* oxidase active site structure, were generated in an attempt to form the first intramolecular H-bonded complexes. Derivatives of the "parent" ligand (^{X}TMPA, TMPA = (tris((2-pyridyl)methyl)amine)) possessing one or two amine pendants preferentially form an H-bond with the copper-bound *O*-atom of the peroxide bridge. This is evidenced by a characteristic blue shift in the ligand-to-metal charge transfer (LMCT) bands observed in UV-vis spectroscopy (consistent with lowering of the peroxo π^* relative to the iron orbitals) and a weakening of the O–O bond determined by resonance Raman spectroscopy (rR), with support from Density Functional Theory (DFT) calculations. Remarkably, with the TMPA-based infrastructure (*versus* similar heme–peroxo–copper complexes with different copper ligands), the typically undetected Cu–O stretch for these complexes was observed *via* rR, affording critical insights into the nature of the O–O peroxo core for the complexes studied. While amido functionalities have been shown to have greater H-bonding capabilities than their amino counterparts, in these heme–peroxo–copper complexes amido substituents distort the local geometry such that H-bonding with the peroxo core only imparts a weak electronic effect; optimal H-bonding interactions are observed by employing two amino groups on the copper ligand. The amino-substituted systems presented in this work reveal a key orientational anisotropy in H-bonding to the peroxo core for activating the O–O bond, offering critical insights into effective O–O cleavage chemistry. These findings indirectly support computational and protein structural studies suggesting the presence of an interstitial H-bonding water molecule in the C*c*O active site, which is critical for the desired reactivity. The results are evaluated with appropriate controls and discussed with respect to potential O_2-reduction capabilities.

Received 19th November 2018
Accepted 3rd January 2019

DOI: 10.1039/c8sc05165h

rsc.li/chemical-science

Introduction

In protein-mediated reactions, hydrogen bonding is well known to be critical for active site chemistry, including directing substrate binding and facilitating key catalytic steps.[1–5] This is especially important for metalloenzymes involved in dioxygen processing (such as in O_2-carriers, oxidases, or oxygenases). For instance, protonation and/or hydrogen bonding is critical in directing O–O bond scission in heme-containing enzymes such as cytochrome P450s, catalases, and peroxidases, by lowering the barrier to O–O reductive cleavage and/or selectively enhancing heterolytic (over homolytic) cleavage.[4,6,7]

Catalytic reduction of O_2 to water by heme–copper oxidases (HCOs) involves $8H^+$ and $4e^-$, wherein $4H^+$ are translocated across the inner mitochondrial membrane, driving ATP synthesis.[5,8–12] The pertinent mammalian terminal respiratory enzyme is cytochrome *c* oxidase (C*c*O), which facilitates O_2 reduction following dioxygen binding to the heterobinuclear active site comprised of a reduced heme (Fe^{II}) and copper (Cu^I) moiety, initially forming the ferric superoxide species (**A**, Scheme 1).[5] In the established catalytic mechanism of C*c*O, the four electrons derive from iron ($2e^-$; $Fe^{II} \rightarrow Fe^{IV}$), copper ($1e^-$;

---

[a] *Department of Chemistry, Johns Hopkins University, Baltimore, Maryland 21218, USA. E-mail: karlin@jhu.edu*

[b] *Department of Chemistry, Stanford University, Stanford, California 94305, USA. E-mail: edward.solomon@stanford.edu*

† Electronic supplementary information (ESI) available: Synthetic and analytical details (methodologies and UV-vis, EPR, NMR, rR, and IR spectra). See DOI: 10.1039/c8sc05165h

‡ These authors contributed equally to this work.

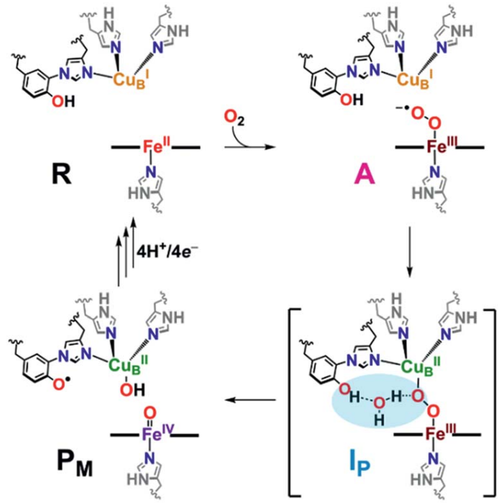

Scheme 1 A portion of the catalytic cycle of cytochrome *c* oxidase, emphasizing the key steps in which H-bonding (highlighted in blue, I_P) mitigates homolytic O_2 reductive cleavage, forming the tyrosyl radical and high valent iron(IV) species (P_M). See text for further discussion.

$Cu^I \rightarrow Cu^{II}$), and a tyrosine residue cross-linked to one His ligand bound to Cu ($1e^-/1H^+$; TyrOH → TyrO$^\bullet$).[5,8,9,11] A unique covalent cross-link between the tyrosine and one of the Cu-bound histidine residues is believed to modulate both the redox potential and the pK_a of the TyrO-H.[13–15] It is also postulated that an H-bonding network of water molecules exists in the active site, linking the TyrOH residue to a putative metal-(hydro)peroxide species (**I_P**), facilitating the necessary proton coupled electron transfer (PCET) from the tyrosine to achieve homolytic O–O cleavage resulting in the formation of the high-valent intermediate **P_M** (Scheme 1). Following a subsequent series of proton (PT) and electron (ET) transfer reactions, also accompanied by membrane proton translocation steps, the initial state of reduced heme and copper (**R**, Scheme 1) reforms providing for the overall release of two mole-equivalents of water from one mole-equivalent O_2.[16–24] Interestingly, H-bonding interactions involving the active site Tyr have also been shown to be important for controlling proton gating and delivery from the K-channel to the active site for complete protonation-reduction of O_2 to H_2O.[16]

Synthetic heme–peroxo–copper model systems can be strategically designed to probe fundamental chemical questions, including the factors that influence reductive O–O cleavage, such as H-bonding and/or proton relay processes. These are often accompanied by electron transfer reactions that result in, and can be applied to, practical catalytic systems; synthetic systems may enhance the understanding of these PT and ET steps to better grasp aspects that may be detrimental to efficiency or longevity. Results from biochemical and computational studies on HCOs, as well as various synthetic heme–peroxo–copper systems, have provided significant insights into Nature's rationale for taking advantage of hydrogen bonding to easily impart significant electronic or geometric alterations to tune the enzymatic active site to facilitate O_2 reduction chemistry (heterolytic *vs.* homolytic cleavage) at metal sites, a biochemical process critical to all aerobic organisms.[17,18,25–27] However, a deeper understanding of how H-bonding impacts O–O cleavage in HCOs is needed, as parts of this mechanism have remained elusive due to the fast kinetics of the homolytic cleavage step (from **A** to **P_M**) in the enzyme, which for example has prevented thorough characterization of a widely proposed $2e^-$-reduced peroxo level intermediate[20,28,29] (**I_P** in Scheme 1, which has recently been supported by experimental and computational studies by Brzezinski, Blomberg, and coworkers)[30] and the subtleties relevant to the further ET, PT or PCET step(s).

While previously reported heme–peroxo–copper model studies have presented a valuable new route for investigating O–O cleavage by observing H-bonding interactions with exogenous substrates,[26,27,31] they are complicated by entropic factors (*i.e.*, bimolecular interactions) not present in the enzyme. Thus, herein we develop intramolecular H-bonding heme–peroxo–copper systems in the hope that mechanistic insights can be gained toward understanding how H-bonding could: (1) stabilize the formation of the proposed, but not spectroscopically observed, **I_P** intermediate,[5,20,30] (2) help gain structural and electronic perspectives on the influence of H-bonding in O_2-reduction chemistries, and (3) further the development of a more biomimetic, C*c*O-inspired, synthetic model in order to do corresponding reactivity studies. The results presented herein provide insights into how the incorporation of intramolecular H-bonding moieties affect the electronic structure and core vibrations of the observed low-spin heme–peroxo–copper complexes. In most cases, density functional theory calculations of the energy-minimized structures accompany the spectroscopic observations and lend support for the conclusions drawn.

Results and discussion

Development of synthetic hydrogen bonding complexes

Mechanistic insights into O_2 activation and reduction from promising reactivity studies of heme–peroxo–copper synthetic systems utilizing the copper ligand TMPA (and also a porphyrinate with a tethered TMPA moiety; TMPA = tris(2-pyridylmethyl)amine) have been reported.[32–43] These include synthesis of reduced heme(Fe^{II})–Cu^I complexes, O_2 reactivity leading to μ-oxo [heme–Fe^{III}–(μ-O^{2-})–Cu^{II}]$^+$ and conjugate acid [heme–Fe^{III}–(μ-OH^-)–Cu^{II}]$^{2+}$ compounds, spectroscopic-structural characterization of discrete peroxo-bridged [heme–Fe^{III}–(μ-O_2^{2-})–Cu^{II}]$^+$ complexes and (electro)catalytic O_2-reduction studies. In this current investigation, a series of Cu(^{X}TMPA) derivatives are paired with tetrakis(2,6-difluorophenyl) porphyrinate (F_8) heme for generation of low-spin heme–peroxo–copper synthetic model complexes [(DCHIm)(F_8)Fe^{III}–(O_2^{2-})–Cu^{II}(TMPA)]$^+$, (DCHIm = 1,5-dicyclohexylimidazole) in 2-methyltetrahydrofuran (MeTHF) solvent under cryogenic conditions (−90 °C, Fig. 1). Most heme-containing metalloenzymes that perform dioxygen chemistry (*e.g.*, catalases, peroxidases, P450's, oxidases, and globins) require a proximal axial base; hence, to generate low-spin species and understand the H-bonding interactions in these heme-based

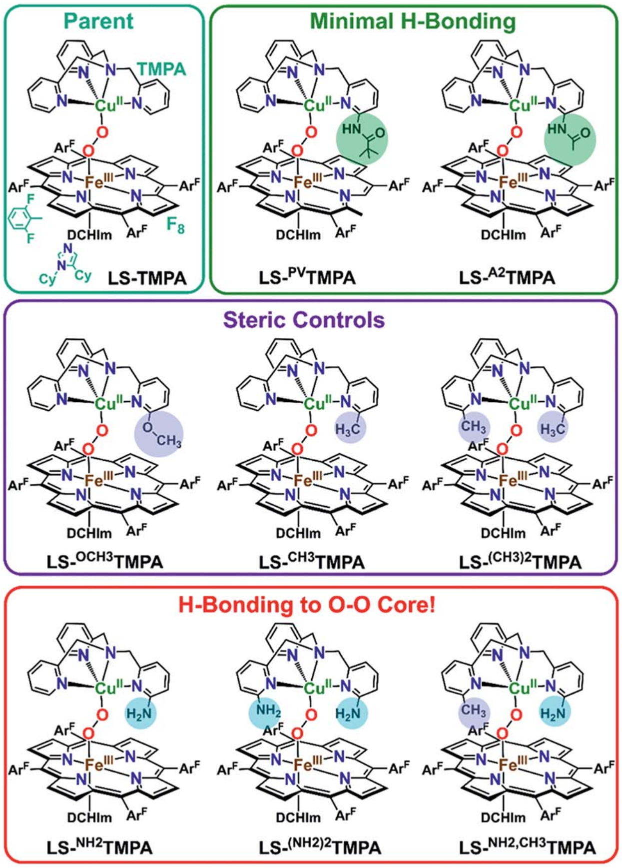

Fig. 1 The established parent TMPA heme–peroxo–copper complex and eight new low-spin heme–peroxo–copper complexes bearing derivatized TMPA-based copper chelates, including those with potential H-bonding modules, whose steric and H-bonding influences are elucidated in this work.

metalloenzyme mimics, the strong electron donating axial base, DCHIm, was employed, mirroring the histidine proximal ligand in C*c*O.

Novel low-spin heme–peroxo–copper synthetic complexes using eight TMPA-derivatized copper ligands (Fig. 1) have been prepared in order to develop a series of compounds that have the potential or do in fact demonstrate significant H-bonding capabilities; H-bonding has previously been shown in copper(II) chloride complexes bearing some of these ligands.[44] A systematic study presented here enables us to examine the effects of secondary coordination sphere substitutions on the structural and electronic properties such as (1) intramolecular H-bonding preference for the Cu–O or Fe–O oxygen-atom, (2) structural variations caused and influencing the dihedral angle of the Fe–O–O–Cu core, (3) changes in Fe–O, Cu–O, and O–O bond lengths, and (4) the impact of one *vs.* two H-bonding functionalities. Taken together, these results are crucial to thinking about how H-bonding dictates reactivity in the enzyme. The use of intramolecular H-bonding amino moieties incorporated on the TMPA ligand template, positioned to enable an interaction with the peroxo core, aims to further understand how H-bonding interactions may facilitate reductive O–O cleavage.

As such, TMPA-based copper ligands, with various substituents in the 6-pyridyl position, were thoughtfully synthesized and utilized: $^{\mathrm{CH3}}$TMPA, $^{\mathrm{(CH3)2}}$TMPA, $^{\mathrm{OCH3}}$TMPA, $^{\mathrm{PV}}$TMPA, $^{\mathrm{A2}}$TMPA, $^{\mathrm{NH2}}$TMPA, $^{\mathrm{(NH2)2}}$TMPA, and $^{\mathrm{NH2,CH3}}$TMPA (Fig. 1; see ESI† for synthetic and characterization details). In particular, comparison of heme–peroxo–copper complexes bearing the ligands $^{\mathrm{NH2}}$TMPA, $^{\mathrm{CH3}}$TMPA, and $^{\mathrm{OCH3}}$TMPA can help differentiate steric *vs.* H-bonding influences; we can rule out electron-donating effects on the basis that the $\mathrm{Cu^{II/I}}$ reduction potential of complexes bearing these ligands are very similar ($E_{1/2} = -0.34$ or -0.35 V) (Fig. S3 & Table S2†), indicating the three ligands donate electron density to the copper ion in a nearly identical manner.§ Another important property is revealed by the present study and data obtained; the metal–oxygen stretching frequencies (especially Cu–O) are typically not observed *via* resonance Raman spectroscopy (rR) in previously studied synthetic heme–peroxo–copper complexes.[36,39,45–48] However, as demonstrated herein (*vide infra*), we have found that systems with the TMPA infrastructure yield strong resonance enhancement of both the Fe–O and Cu–O stretches, offering unique and valuable insights into the bonding in the heme–peroxo–copper core.

Azido-Cu(II) complexes to assess ligand H-bonding capabilities

To assess the H-bonding capabilities of these ligands, the azido complexes, $[(^{\mathrm{X}}\mathrm{TMPA})\mathrm{Cu^{II}}(\mathrm{N_3}^-)]^+$, many of which were previously reported and characterized by X-ray crystallography by Masuda and coworkers (Fig. 2),[49,50] were prepared and, for the first time, analyzed by IR spectroscopy to observe steric, electronic, or H-bonding influences on the vibrational stretching frequency characteristic of the $\mathrm{N_3}^-$ moiety (Fig. 3 and S2 and Table S1†). Substitution of an amino moiety on the TMPA framework, $[(^{\mathrm{NH2}}\mathrm{TMPA})\mathrm{Cu^{II}}(\mathrm{N_3}^-)]^+$, *vs.* the parent TMPA azido complex showed that the former possesses a higher ν(N–N) stretching frequency by 10 $\mathrm{cm^{-1}}$ (Fig. 3A and Table S1†). Addition of a second amino group, in $[(^{\mathrm{(NH2)2}}\mathrm{TMPA})\mathrm{Cu^{II}}(\mathrm{N_3}^-)]^+$, further increased the ν(N–N) by 8 $\mathrm{cm^{-1}}$ (18 $\mathrm{cm^{-1}}$ greater than the parent TMPA azido complex) (Fig. 3A and Table S1†), consistent with previously reported X-ray structures[50] that showed H-bonding to the proximal (bound to Cu) N-atom of the azido ligand (with $\mathrm{N(H)\cdots N_{azido}}$ distances of 2.93 and 2.95 Å and $\angle \mathrm{NHN_{azido}} = 146.1$ and 158.1° observed for $[(^{\mathrm{(NH2)2}}\mathrm{TMPA})\mathrm{Cu^{II}}(\mathrm{N_3}^-)]^+$).

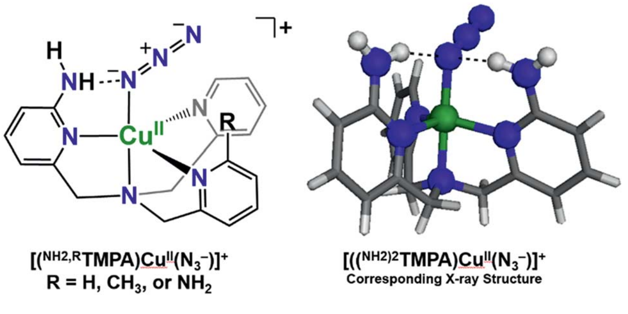

Fig. 2 H-bonding interactions of cupric azido complexes observed *via* X-ray crystallography by Masuda and coworkers.[50]

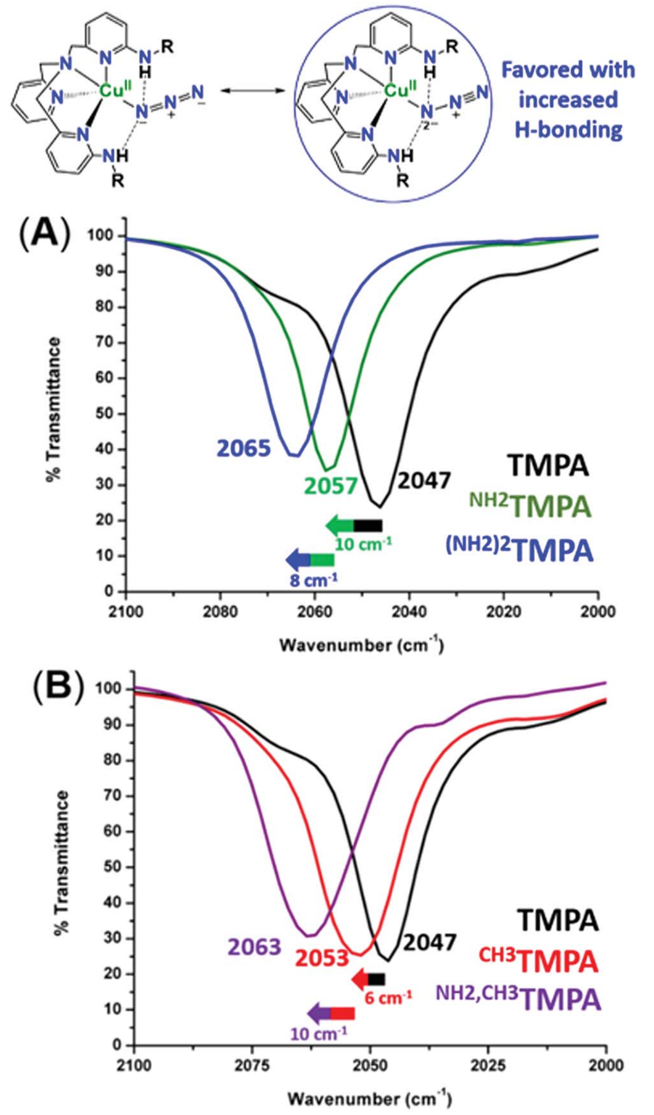

Fig. 3 Infrared spectra of $[(^{X}TMPA)Cu^{II}(N_3^-)]^+$ complexes in CH_3CN, showing the increase of the ν(N–N) stretch upon incorporation of amino substituents (A) and incorporation of steric functionalities (B).

As evidenced by comparing the ν(N–N) values for the cupric azido complexes bearing the ligands ^{NH2}TMPA and TMPA (Fig. 3A) *vs.* ^{NH2,CH3}TMPA and ^{CH3}TMPA (Fig. 3B), the ^{NH2}TMPA and ^{NH2,CH3}TMPA ligands have the same H-bonding capabilities (each shows a 10 cm^{-1} blue-shift when compared to their respective "base" ligand). The azido derivative with ^{CH3}TMPA has a ν(N–N) value slightly higher than with TMPA, implicating a negligible steric influence (Fig. S2A & Table S1†). The ^{PV}TMPA cupric azido complex has a ν(N–N) stretching frequency similar to $[(^{(NH2)2}TMPA)Cu^{II}(N_3^-)]^+$ (within 1 cm^{-1}, Fig. S2B & Table S1†), suggesting that one pivalamido group can exert an H-bonding strength roughly equivalent to two $-NH_2$ groups.

Masuda and coworkers also previously showed that some of the same H-bonding copper ligands utilized herein (^{PV}TMPA, ^{NH2}TMPA, and $^{(NH2)2}$TMPA) provide for enhanced stability of dicopper(II) *trans*-peroxide complexes complexes (Fig. 4) due to H-bonding to the peroxo core.[49,50] Further, ^{PV}TMPA has also been shown to stabilize a cupric superoxide complex (*vide infra*).[51]

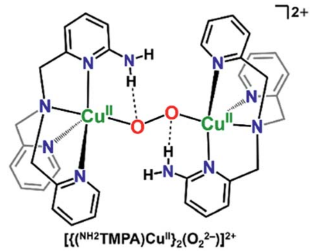

Fig. 4 H-bonding interactions enhance the stability of dicopper(II) *trans*-peroxide complexes as reported by Masuda and coworkers.[50]

Thus, we hypothesized that amino functionalities may stabilize a heterobinuclear peroxide complex as well, and thereby generate good systems to carry out future reactivity studies; one would expect the barrier to reduce the O–O bond would be less if H-bonding caused bond elongation. Therefore, these interactions may facilitate O_2-reduction chemistry by these systems. Ligands bearing methyl (^{CH3}TMPA & $^{(CH3)2}$TMPA) or methoxy substituents (newly synthesized ^{OCH3}TMPA) (Fig. 1) were included in the series to serve as appropriate controls, wherein the methyl groups or methoxy group may influence the Cu-geometry in a similar manner as in the other derivatives, however without any hydrogen bonding interaction. The mixed derivative, ^{NH2,CH3}TMPA, was newly synthesized (Fig. S1†)§ to probe whether both amino moieties in **LS-$^{(NH2)2}$TMPA** interact with the O–O peroxo core (and to assess if the second amino group doubles the magnitude of the H-bonding effects or interacts to a lesser degree).

Results collected in this work, further described below, (1) demonstrate the balance between sterics and H-bonding in developing appropriate synthetic systems to model behaviors featured in metalloenzymes, (2) establish the importance of corresponding controls in verifying novel synthetic models, and (3) show evidence supporting the H-bonding capabilities of the *Cc*O-inspired low-spin heme–peroxo–copper complexes bearing the ligands ^{NH2}TMPA, $^{(NH2)2}$TMPA, and ^{NH2,CH3}TMPA.

Synthesis and UV-vis spectroscopic characterization

The spectroscopic properties of the title compounds are evaluated in the context of established (heme-)copper chemistry.[26,27,33,36,37,52–56] Following well-known procedures, the high-spin heme–peroxo–copper complexes ($[(F_8)Fe^{III}-(O_2^{2-})-Cu^{II}(^{X}TMPA)]^+$, Fig. S4†) were generated by bubbling dioxygen through an equimolar mixture of the reduced metal–ligand complexes (Fig. 5 and S4†);[36] these all are stable at −90 °C in MeTHF, where the $[(^{X}TMPA)Cu^{I}]^+$ precursors utilized were $B(C_6F_5)_4^-$ (≡BArF) salts.§ Addition of one equivalent of DCHIm affords the corresponding low-spin analogs $[(DCHIm)(F_8)Fe^{III}-(O_2^{2-})-Cu^{II}(^{X}TMPA)]BArF$ (**LS-^{X}TMPA**, Fig. 1 and 5) which are the focus of this work as most heme metalloenzymes can only function with (and depend on) a proximal axial base.[5,6,28]

The binding mode of the peroxide ligand in the parent **HS-TMPA** complex has been previously well established to

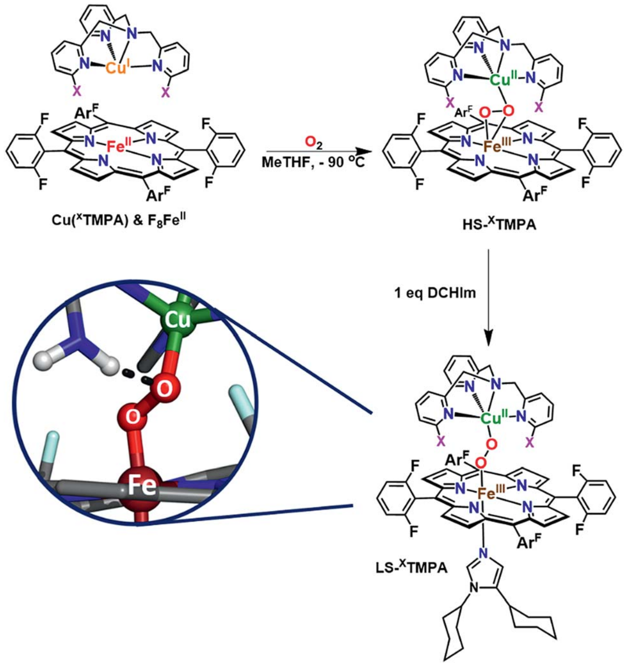

Fig. 5 Established synthetic approach for heme–peroxo–copper complexes, wherein addition of dioxygen to the reduced iron and copper complexes (in a 1 : 1 stoichiometry) results in formation of the high-spin complexes, **HS-^{X}TMPA**. Addition of 1 equiv. of 1,5-dicyclohexylimidazole (DCHIm, which acts as an axial base) affords low-spin heme–peroxo–copper species (**LS-^{X}TMPA**, with *X* as depicted in Fig. 1). As shown in the bottom left inset (as one possible example of the present study), we are investigating the influence of H-bonding on the peroxo core.

possess a μ-η^2:η^1 (side-on to iron, end-on to copper) bridge (Fig. 5), based on a great deal of spectroscopic data, DFT calculations, and precedent from an early X-ray structure of an analog compound characterized by Naruta and coworkers.[33,40,57,58] The high-spin state of the parent heme–peroxo–copper complex **HS-TMPA** (overall $S = 2$) was also previously confirmed by the rR spin state marker band, ν_2,[31] by ^{2}H-NMR spectroscopy (observation of a paramagnetic peak using pyrrole-deuterated F_8 porphyrin)[59] and *via* EPR spectroscopy (the observed X-band silent spectrum was ascribed to antiferromagnetic coupling between the iron and copper ions).[59] The peroxo binding mode in the low-spin heme–peroxo–copper complex **LS-TMPA** (Fig. 5) was previously determined to be end-on to both copper and iron (*trans*-μ-η^1:η^1) based on the combination of spectroscopic data, DFT calculations, and analogy to previously characterized low-spin species.[36] Based on DFT energy-minimized structures for HS- *vs.* **LS-TMPA**,[33,37,59,60] the end-on formulation in the low-spin species also results in an elongated metal–metal distance (**HS-TMPA:** $r(\text{Fe}\cdots\text{Cu}) = 3.982$ Å (3.72 Å by EXAFS),[37] **LS-TMPA:** $r(\text{Fe}\cdots\text{Cu}) = 4.485$ Å).

Eight high-spin heme–peroxo–copper complexes $[(F_8)Fe^{III}–(O_2^{2-})–Cu^{II}(^XTMPA)]^+$ were newly generated at −90 °C in MeTHF (structures depicted in Fig. S4†), and subsequent UV-vis monitoring of their formation indicated they all had comparable spectra with a Soret ~416 nm and a split Q-band $\lambda_{max} \sim 560$ nm and a diagnostic ~650 nm absorption feature (a porphyrin to iron transition often called CT2 in heme literature)[61] regardless of the TMPA substituent (Table 1, Fig. S5 and S6† in blue). Due to the comparable UV-vis spectra of these **HS-^{X}TMPA** complexes, $[(F_8)Fe^{III}–(O_2^{2-})–Cu^{II}(^XTMPA)]^+$ (Fig. S4–S6†), the paramagnetic ^{2}H-NMR shifts observed (Fig. S7† in blue), and their silent EPR spectra, these new species were confirmed to be high-spin. It is of note that the similar UV-vis spectra, paramagnetic ^{2}H-NMR signal, and silent EPR spectra (X-band) are consistent with many other high-spin heme–peroxo–copper complexes previously reported (not just with **HS-TMPA**).[27,36,53,59,62]

The UV-vis spectra show a red shift in both the Soret (~7–12 nm) and Q-band (~27 nm) after addition of one equivalent of DCHIm (Fig. 5) to the **HS-^{X}TMPA** complexes (Fig. S5 and S6† in green), consistent with previously reported shifts of synthetic heme–peroxo–copper complexes going from HS to **LS-^{X}TMPA** species.[26,36,62] Thus, with eight new HS (Fig. S4†) and then eight corresponding LS complexes, a total of sixteen new heme–peroxo–copper species are described here. However, this work focuses particularly on the imidazole-ligated low-spin complexes, which possess a heme structure comparable to the C*c*O binuclear active site (Fig. 1). The low-spin state ($S = 0$) of these novel **LS-^{X}TMPA** complexes was confirmed by the rR spin state marker band, ν_2 (Table 1),[31] by a diamagnetic ^{2}H-NMR signal from employing the d_8(pyrrole)-F_8 analog (*i.e.*, $[(DCHIm)–(d_8F_8)Fe^{III}–(O_2^{2-})–Cu^{II}(^XTMPA)]$BArF, thus the observed signal is from the pyrrole deuterons, Fig. S7† in green), and from silent EPR spectra being observed for all the complexes, indicating antiferromagnetic coupling between the low-spin iron(III) and copper(II) sites, mediated by the peroxo bridging ligand. These findings are consistent with the previous spectral characterization of the parent heme–peroxo–copper complex **LS-TMPA**.[36,40,59] The UV-vis spectral changes from the high-spin to low-spin species in each case are analogous to those reported for similar model complexes (*vide infra*), which have been shown to be concomitant with a change in binding mode from μ-η^2:η^1 to *trans*-μ-η^1:η^1.[26,27,33,36,37,59,60] Therefore, we propose at this time that the core peroxo binding mode in the novel **LS-^{X}TMPA** complexes is also end-on coordinated to both metal ions, as depicted in Fig. 1 and 5.

All of the **LS-^{X}TMPA** complexes have similar UV-vis spectral features with a Soret absorption around 425 nm and a Q-band λ_{max} around 533 nm regardless of the Cu ligand identity (Fig. S5 & S6,† Table 1); however, the absorption bands observed at lower energy show variation in both wavelength and intensity (Fig. 6 and S6† & Table 1). These unique low energy bands have been attributed to peroxo-to-Fe charge transfer (CT) transitions and serve as a diagnostic fingerprint for all synthetic low-spin heme–O_2^{2-}–Cu species of this nature characterized to date,[36,63] providing valuable evidence confirming the low-spin state and showing how variations in Cu ligand substitution influence the peroxo core. Relative to the parent **LS-TMPA** and the steric control compounds, **LS-^{CH3}TMPA**, **LS-$^{(CH3)2}$TMPA**, and **LS-^{OCH3}TMPA**, the CT bands for **LS-^{NH2}TMPA**, **LS-$^{(NH2)2}$TMPA**, and **LS-^{NH2,CH3}TMPA** are observed at higher energy (*i.e.*, amine substitution on the pyridyl donor(s) results in a blue shift; this ligand-to-metal charge transfer (LMCT) blue shift has also been previously reported by Masuda and coworkers for the copper(II)-

Table 1 Spectroscopic properties of low-spin heme–peroxo-complexes with TMPA-derived copper chelates (br = broad; f.d. = Fermi doublet)[a]

$(DCHIm)F_8Fe^{III}–O_2–Cu^{II}(L)$, Identity of **L**	UV-vis (nm)	Raman $^{16}O_2$ (cm^{-1})			
		ν(O–O)	ν(Fe–O)	ν(Cu–O)	$\nu_2;\nu_4$
TMPA	426, 535, 850, 950, 1020 (br)	812	623	535	1572; 1364
^{NH2}TMPA	426, 536, 790, 900 (br)	775	625	533	1570; 1364
$^{(NH2)2}$TMPA	425, 538, 785, 870 (br)	760	614	506	1571; 1367
^{NH2,CH3}TMPA	425, 533, 789, 897 (br)	765	610	510	1571; 1367
^{CH3}TMPA	422, 534, 855, 980 (br)	789 (f.d.)	612	525	1570; 1363
$^{(CH3)2}$TMPA	420, 538, 845, 940 (br)	776	593	501	1570; 1363
^{PV}TMPA	429, 536, 840 (br)	806	573	489	1571; 1365
^{A2}TMPA	426, 535, 823 (br)	802	580	484	1571; 1366
^{OCH3}TMPA	424, 539, 853, 946 (br)	805	575	483	1569; 1365

[a] See the ESI for the UV-vis spectra (Fig. S5 and S6) and for the ($^{16}O_2$–$^{18}O_2$) data and raw rR spectra (Fig. S8).

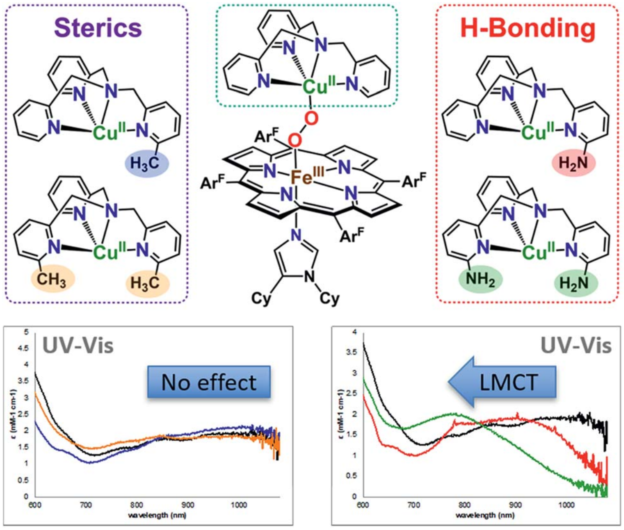

Fig. 6 Zoomed in UV-vis spectra of the low-energy region (~700–1000 nm) for the low-spin heme–peroxo–copper complexes with various TMPA-based copper ligands, demonstrating the characteristic blue shift observed with substituents that H-bond to the O–O peroxo core. Bottom left: **LS-TMPA** (black), **LS-^{CH3}TMPA** (blue), and **LS-$^{(CH3)2}$TMPA** (orange). Bottom right: **LS-TMPA** (black), **LS-^{NH2}TMPA** (red), and **LS-$^{(NH2)2}$TMPA** (green).

azido and dicopper(II) *trans*-peroxo complexes bearing the ligands ^{NH2}TMPA and $^{(NH2)2}$TMPA).[49,50] This is attributed to the H-bond interaction lowering the peroxo π* donor orbital energies more than the Fe acceptor orbitals (see Fig. 6, S6† & Table 1). Importantly, this diagnostic marker, the blue shift of the low energy absorption λ_{max}, increases systematically with the number of $–NH_2$ substituents (Fig. 6, S6† & Table 1), providing compelling evidence that all $–NH_2$ groups employed interact with the peroxo core. In line with these trends, **LS-^{NH2,CH3}TMPA** shows low energy features similar to **LS-^{NH2}TMPA**, while those of **LS-$^{(NH2)2}$TMPA** are shifted to even higher energy, suggesting that both amino groups of **LS-$^{(NH2)2}$TMPA** are H-bonding to the O–O peroxo core and that it is not due to the additional sterics from incorporating a second functionality on the TMPA framework (Fig. 6, S6† & Table 1). These conclusions about H-bonding to the peroxo core by the ligand-amino pendants are supported by resonance Raman spectroscopic interrogation (*vide infra*).

Masuda and co-workers[49] previously demonstrated increased H-bonding capabilities from ^{PV}TMPA (with pivalamido potential H-bonding moiety (Fig. 1)) relative to ^{NH2}TMPA by comparing their respective dicopper(II) *trans*-peroxide complexes; this is expected since –pivalamido groups are more acidic than –amino substituents. Thus, to optimize the amount of H-bonding interactions between the intramolecular functionality and the O–O peroxo core, the low-spin heme–peroxo–copper complex with ^{PV}TMPA (*i.e.*, $[(DCHIm)(F_8)Fe^{III}–(O_2^{2-})–Cu^{II}(^{PV}TMPA)]BArF$, **LS-^{PV}TMPA**) was synthesized (Fig. 1). The UV-vis spectrum exhibits similar Soret (429 nm) and Q-band λ_{max} (533 nm) absorptions as all the other **LS-^{X}TMPA** derived complexes (Table 1), however, the low-energy region exhibits uniquely one broad intense peak around 840 nm (Fig. S5G, S6G† & Table 1). While this effect could indicate H-bonding to the peroxo core, it is notable that this low-energy band for **LS-^{PV}TMPA** is markedly more intense than observed for the other **LS-^{X}TMPA** complexes ($\varepsilon \sim 6000\ mM^{-1}\ cm^{-1}$ *vs.* 2000–4000 $mM^{-1}\ cm^{-1}$). This deviation may indicate a structural change (or distortion of the dihedral Fe–O–O–Cu angle), that is likely imparted by the presence of the very bulky *tert*-butyl group. To probe this possibility, a new ligand with a less bulky carbonyl substituent (a methyl instead of a *tert*-butyl group) was synthesized (^{A2}TMPA, with a 6-pyridyl –acetylamido moiety) and the corresponding DCHIm-bound low-spin heme–peroxo–copper complex was prepared (Fig. 1). The UV-vis spectrum of this complex ($[(DCHIm)(F_8)Fe^{III}–(O_2^{2-})–Cu^{II}(^{A2}TMPA)]BArF$, **LS-^{A2}TMPA**) was similar to **LS-^{PV}TMPA**, exhibiting one broad, intense low-energy feature around 823 nm (Fig. S5F, S5G, S6F and S6G,† Table 1). This indicates that the amido functionality impacts the peroxo core in a manner that is distinct from amino or methyl groups alone, potentially arising from variation in the geometric and electronic structure around the Cu (*vide infra*). This finding demonstrates the careful balance between sterics and electronics (*i.e.*, H-bonding) in our synthetically derived heme–peroxo–Cu complexes (highlighting the intricacies in developing synthetic models), which nature has also mastered in its design of metalloenzymes in order to dictate biologically required catalytic transformations.

These diagnostic low-energy CT bands (Fig. 6 & S6† and Table 1) provide valuable evidence for how variations in Cu ligand substitution influence the peroxo core and offer indirect evidence for intramolecular H-bonding interactions for the three novel low-spin heme–peroxo–copper complexes containing amino groups (**LS-^{NH2}TMPA**, **LS-$^{(NH2)2}$TMPA**, and **LS-^{NH2,CH3}TMPA**, Fig. 1), and potentially two amido-containing complexes (**LS-^{PV}TMPA** and **LS-^{A2}TMPA**, Fig. 1). As other research labs, such as those of Masuda, Nocera, and Dey,[50,64–67] have demonstrated inter- and intramolecular H-bonding in dicopper–peroxide and heme (hydro)peroxide complexes through the use of resonance Raman spectroscopy, we have therefore also evaluated our new low-spin heme–peroxo–copper complexes (Fig. 1) using rR spectroscopy and corresponding computational analysis (*vide infra*).

Impact of H-bonding and sterics on M–O and O–O bonds in the peroxo core as determined from rR spectroscopy

Insight into the effect of these H-bonding interactions is provided by rR spectroscopy, which can serve as a valuable probe of O–O and M–O bond strengths, and distinguish between H-bonding to the proximal or distal O-atom (with respect to Fe).[26,27,68,69] Importantly, we find that significant differences in the rR data for these low-spin complexes are observed (*vide infra*) as a consequence of the derivatization of the TMPA ligands as outlined in Fig. 1.

Among both high-spin and low-spin synthetic model complexes compiled from 15 reports in the literature, a Cu–O stretch has been observed in only three LS species out of 24 HS and LS complexes.[36,39,45,46,48,53,55,56,59,70–75] Further, of those three, only one employed a copper ligand that was not TMPA (the other two being the HS and LS parent TMPA complexes).[36,59,72] Thus, this report more than doubles the description and characterization of known synthetic low-spin heme–peroxo–copper complexes in the literature, with 8 newly prepared species. The remarkably strong resonance enhancement of both the Fe–O and Cu–O stretches with the TMPA ligand may be due to vibrational coupling and/or the presence of an LMCT band masked by the Soret absorption used for excitation. Thus, the rR data on these complexes with derivatized TMPA ligands afford critical insights into the nature of the O–O peroxo core.

It is highly relevant to note that in order to mimic the unique tyrosine–histidine crosslink coordinated to the copper ion in *C*cO, the Karlin and Naruta labs, separately, have reported on synthetic heme–peroxo–copper complexes with a phenol-imidazole crosslink moiety (Fig. 7).[70,74] Interestingly, no H-bonding interactions were observed between the phenol and peroxo core, based on rR spectroscopic data (*i.e.*, no effect on the O–O vibrational frequency was observed). This would likely also be the case in the *C*cO active site, where the nearby tyrosine residue is too far away (~6 Å) to directly H-bond to the O–O peroxo core of a putative $\mathbf{I_P}$ intermediate (Scheme 1). However, an H-bonded network of interstitial water molecules has been suggested, in many computational studies,[28,76,77] to provide the means for proton transfer (from tyrosine) and to facilitate O_2 reductive cleavage. Addressing the growing interest in understanding possible interactions with such active site water molecules, this study presents the first demonstration of intramolecular hydrogen bonding in a synthetic heme–peroxo–copper model system incorporating H-bonding groups.

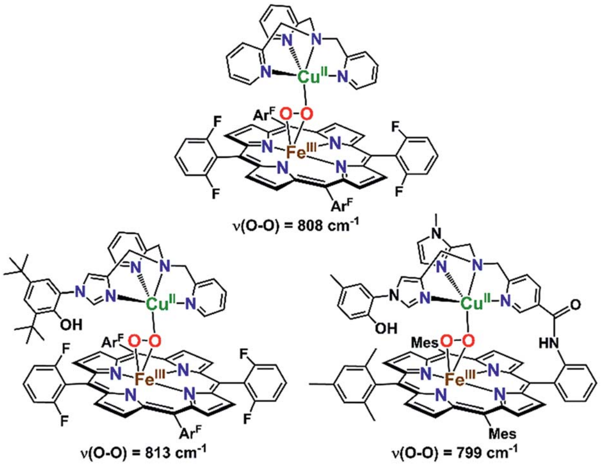

Fig. 7 Previously reported high-spin heme–peroxo–copper complexes and their O–O vibrational frequencies as detected by rR spectroscopy. Incorporation of the phenol-imidazole moiety (*vs.* the parent TMPA complex) showed a similar ν(O–O) stretch, suggesting the phenol is too far away to directly interact with the peroxo core (similar to what is observed in *C*cO), providing indirect evidence for an interstitial water.

As mentioned, significant differences were observed in the rR data (Fig. 8 and S8† and Table 1)¶ for these low-spin complexes with derivatized TMPA ligands (*i.e.*, **LS-XTMPA**, Fig. 1). The data indicate that increasing steric factors (*i.e.*, the presence of ligand methyl-substituents) consistently results in weaker O–O, Fe–O, and Cu–O bonds, based on the progressively lower bond stretches observed for **LS-TMPA** *vs.* **LS-^{CH3}TMPA** *vs.*

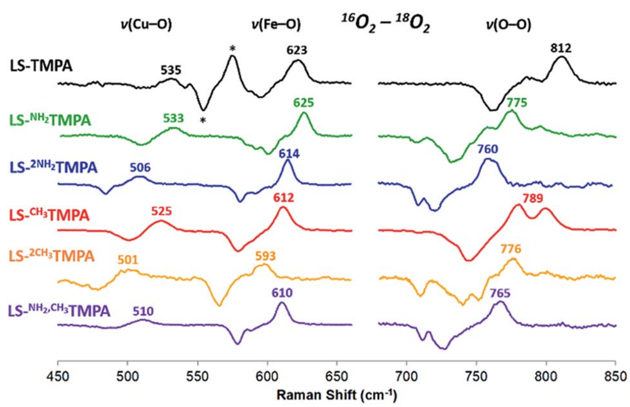

Fig. 8 Comparison of rR data ($^{16}O_2$–$^{18}O_2$) for the LS-^{X}TMPA complexes, which are normalized to equal ν(Fe–O) and ν(O–O) intensities to aid in visual comparison. Isotope-sensitive features are labelled by their frequency in $^{16}O_2$. Note that some modes (*e.g.* 789 cm^{-1} in red spectrum) are split by Fermi coupling. Asterisks (*) denote a ferric superoxo impurity. Laser excitation was 413 nm or 780–890 nm, see ESI.†

LS-$^{\mathrm{(CH3)2}}$TMPA, as well as **LS-$^{\mathrm{NH2}}$TMPA** *vs.* **LS-$^{\mathrm{NH2,CH3}}$TMPA** (Fig. 8, S8A–C, & S8E,† and Table 1). In contrast, substitution of an H-bonding amino group into the complex (*i.e.*, **LS-TMPA** *vs.* **LS-$^{\mathrm{NH2}}$TMPA**, **LS-$^{\mathrm{NH2,CH3}}$TMPA**) appears to minimally impact the Fe–O and Cu–O bond strengths, while greatly weakening the O–O bond. This is a particularly important finding, as a similar decrease in the ν(O–O) vibrational frequency was observed for an H-bonded adduct between a heme–peroxo–Cu model complex and an exogenous phenol (a shift from 870 to 827 cm^{-1} upon addition of *p*-nitrophenol, Scheme 2).[26]

The differences observed between **LS-$^{\mathrm{CH3}}$TMPA** and **LS-$^{\mathrm{NH2}}$TMPA** are attributable to H-bonding in the latter, since there is no electronic difference between the two ligands (as determined from Cu$^{\mathrm{II/I}}$ reduction potentials, as mentioned above§). Interestingly, incorporating a second H-bonding group (as in **LS-$^{\mathrm{(NH2)2}}$TMPA**) acts to weaken all three core modes (Fig. 8 and S8D,† & Table 1) and in fact yields the lowest ν(O–O) among the complexes studied herein.

Resonance Raman data for **LS-$^{\mathrm{PV}}$TMPA** showed significantly lower ν(Fe–O) and ν(Cu–O) modes (573 cm^{-1} and 489 cm^{-1}, respectively), compared to values for **LS-TMPA**, but a relatively high ν(O–O) (806 cm^{-1}), close to that for **LS-TMPA** (812 cm^{-1}, Fig. S8G† and Table 1). The less sterically hindered amido-substituted complex **LS-$^{\mathrm{A2}}$TMPA** nevertheless yielded similar rR data to **LS-$^{\mathrm{PV}}$TMPA** (Fig. S8F† and Table 1), suggesting that these two complexes impact the peroxo core in a comparable manner. However, the rR data obtained for **LS-$^{\mathrm{OCH3}}$TMPA** (steric control bulkier than $^{\mathrm{CH3}}$TMPA) are remarkably similar to **LS-$^{\mathrm{PV}}$TMPA** and **LS-$^{\mathrm{A2}}$TMPA**, including isotope-sensitive modes as well as heme bands (Fig. S8H† and Table 1), suggesting that the effects of the $^{\mathrm{PV}}$TMPA ligand on the peroxo core involve little or no H-bonding, but are predominantly steric in nature.

Further, valuable information is provided by resonance Raman data profiled over the low energy (700–900 nm) region (with excitation at various wavelengths, Fig. S9†). In particular, the complexes **LS-$^{\mathrm{(NH2)2}}$TMPA** and **LS-$^{\mathrm{NH2,CH3}}$TMPA** show preferential enhancement of the ν(Fe–O) and ν(O–O) modes at lower energy excitation, with enhancement of the ν(Cu–O) and ν(Fe–O) (and some ν(O–O)) observed at higher energy excitation. This indicates the presence of two distinguishable LMCT absorption bands (illustrated for **LS-$^{\mathrm{(NH2)2}}$TMPA** in Fig. S10†), wherein the lower energy transition involves excitation from a peroxo orbital that is donating primarily into Fe, while the higher energy transition involves a peroxo orbital donating into both metals. While the remaining complexes studied herein did not exhibit rR profiles indicating two distinct bands, it is worth noting that the complexes **LS-$^{\mathrm{PV}}$TMPA** and **LS-$^{\mathrm{A2}}$TMPA** yielded exceptionally strong ν(Fe–O) and ν(O–O) enhancement, but very weak Cu–O enhancement, suggesting primarily O_2^{2-} to Fe CT character.

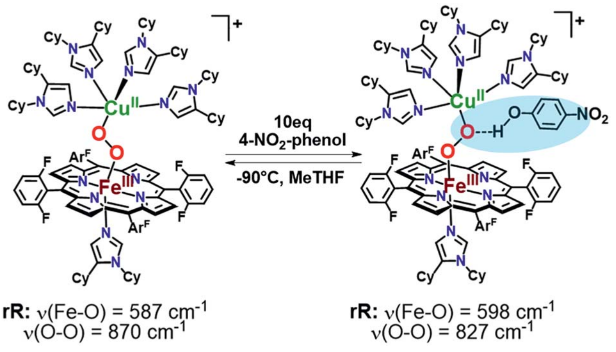

Scheme 2 Previously reported hydrogen-bonding adduct that formed upon addition of 10 equivalents of 4-nitrophenol to a low-spin heme–peroxo–copper complex. Resonance Raman results reported were consistent with the rR in this work (Table 1), where a decrease is observed in the ν(O–O) when H-bonding groups interact with the peroxo core.

It is valuable to note that our analysis leading to the conclusion that the pivalamido group in **LS-$^{\mathrm{PV}}$TMPA** does not or only weakly H-bonds to the peroxo bridging ligand (and see the DFT calculations, below) stands in strong contrast to what we know for the cupric superoxo complex (without any heme present) with the $^{\mathrm{PV}}$TMPA ligand, Fig. 9.[51,78] The reduced copper(I) complex, $[(^{\mathrm{PV}}\mathrm{TMPA})\mathrm{Cu^{I}}]^{+}$ reacts with O_2 at or below −125 °C in MeTHF giving $[(^{\mathrm{PV}}\mathrm{TMPA})\mathrm{Cu^{II}}(O_2^{\bullet-})]^{+}$ with rR stretching values of $\nu(\mathrm{Cu{-}O}) = 482$ $\{\Delta^{18}O_2 = -20\}$ cm^{-1} and $\nu(\mathrm{O{-}O}) = 1130$ $\{\Delta^{18}O_2 = -63\}$ cm^{-1}, clearly shifted significantly from the values for the parent superoxide complex $[(\mathrm{TMPA})\mathrm{Cu^{II}}(O_2^{\bullet-})]^{+}$ possessing no H-bonding modalities, $\nu(\mathrm{Cu{-}O}) = 463$ $\{\Delta^{18}O_2 = -20\}$ and $\nu(\mathrm{O{-}O}) = 1119$ $\{\Delta^{18}O_2 = -61\}$ cm^{-1}.[51] Fig. 9 depicts the structure assigned to $[(^{\mathrm{PV}}\mathrm{TMPA})\mathrm{Cu^{II}}(O_2^{\bullet-})]^{+}$ based on DFT calculations and other spectroscopic or physical characterization. Clearly, the presence of the heme moiety laying in close proximity to the pivalamido *tert*-butyl group in **LS-$^{\mathrm{PV}}$TMPA**, inhibits H-bonding, *vide infra*.

Electronic insights from DFT calculations: orbital considerations for H-bonding effects

In order to better understand how hydrogen bonding impacts the heme–peroxo–copper core, DFT calculations were performed to correlate to the spectroscopic data. Geometry optimization for **LS-TMPA**‖ and **LS-$^{\mathrm{NH2}}$TMPA** reveals distinct changes in the O–O, Fe–O, and Cu–O bond lengths that provide good agreement with the trends observed in the rR data (Table 1). Analytical frequency calculations support the observed trends, although vibrational modes are often highly mixed in the calculations. Therefore, predicted changes in vibrational frequency were also computed based on calculated structural changes using Badger's Rule (Table S3†), providing a direct correlation between bond length and stretching frequency for two-atom-centered vibrational modes.

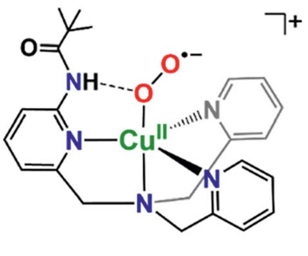

Fig. 9 Intramolecular H-bonding interactions in cupric superoxo complexes, such as in $[(^{\mathrm{PV}}\mathrm{TMPA})\mathrm{Cu^{II}}(O_2^{\bullet-})]^{+}$ depicted here, result in enhanced reactivity towards phenolic (O–H) substrates.[51,78]

To evaluate how the –NH_2 group in **LS-^{NH2}TMPA** interacts with the peroxo core, four principle orientations were considered, wherein the H-bond is directed toward either O_{Cu} (Fig. 10A and 10B) or O_{Fe} (Fig. S10A and B†), and interacting *via* the $O_2{}^{2-}$ π^*_v (perpendicular to Fe–O–O plane, Fig. 10A, 11B & S11A†) or the $O_2{}^{2-}$ π^*_σ (in the Fe–O–O plane, forming the metal-O σ-bonds, Fig. 10B, 11A & S11B†) orbital. Based on the calculations, binding to the O_{Cu} atom is favored by ~2 kcal mol^{-1} (*vs.* O_{Fe}), and results in a *substantially weaker* O–O bond, slightly *weaker* Cu–O bond, and slightly *stronger* Fe–O bond, relative to **LS-TMPA** (consistent with the rR data). In contrast, H-bonding to the O_{Fe} substantially weakens the Fe–O bond and strengthens the Cu–O bond, which does not correlate with the actual rR data obtained. Calculations show that H-bonding *via* the O_2 π^*_v orbital is favored by ~5 kcal mol^{-1} (*vs.* O_2 π^*_σ), although it is of note that both interactions yield similar effects (but greater in magnitude for O_2 π^*_v binding). Taken together, these results suggest that the –NH_2 moiety in **LS-^{NH2}TMPA** H-bonds to O_{Cu} *via* the π^*_v orbital (Fig. 11B).

To fully understand how the H-bonding interaction impacts the core vibrations, we evaluated both structural and electronic consequences of the H-bond to the O_2 π^*_v orbital. Regarding the structural effects of H-bonding in **LS-^{NH2}TMPA**, the peroxo core rearranges to a more obtuse dihedral angle (from Fe–O–O–Cu = 141° in **LS-TMPA** to 152° in **LS-^{NH2}TMPA**, Fig. S12†), orienting the H-bond vector to be nearly orthogonal to both M–O bonds (minimizing its impact on peroxo-to-metal σ donation). While the wider Fe–O–O–Cu dihedral angle would decrease O–O π^*_σ donation into Fe due to competition with donation (α-spin) into Cu, it orients the $O_2{}^{2-}$ π^* orbitals to more efficiently overlap both Fe d_{z^2} and dπ orbitals, which would increase donation into Fe.

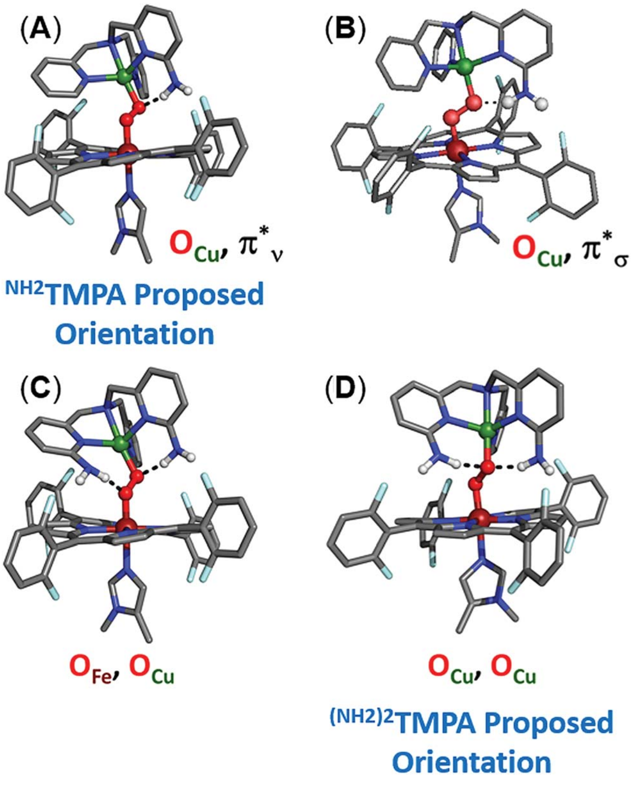

Fig. 10 Optimized DFT structures of LS-^{NH2}TMPA (top: (A) and (B)) and LS-$^{(NH2)2}$TMPA (bottom: (C) and (D)) indicating which orientation of the –NH_2 moieties is preferred in H-bonding to the peroxo core.

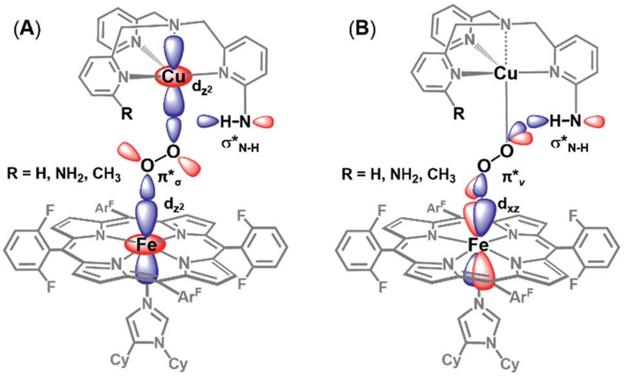

Fig. 11 Orbital diagram for the interaction of the H-bonding amino moiety with the π^* orbitals (π^*_σ, (A), π^*_v, (B)) of the peroxo core. The latter (B) interaction is found to be the most important, see the text.

With respect to the electronic effects, the H-bond lowers the energy of the peroxo π^* orbitals and decreases donation into both metals, resulting in a net transfer of electron density from Fe and Cu to $O_2{}^{2-}$, which weakens the O–O bond. However, the π^*_σ orbital (which donates into both the Fe d_{z^2} (α/β) and Cu d_{z^2} (α), where α-spin Fe is antiferromagnetically coupled to β-spin Cu), exhibits a slight increase in donation into Fe. Since the σ donation from $O_2{}^{2-}$ contributes more to the Fe–O bond strength than π donation (which decreases with H-bonding), the overall effect of the H-bond is to strengthen the Fe–O bond. Taken together, these findings demonstrate that the impact of H-bonding to the O_{Cu} atom of the peroxo core observed in **LS-^{NH2}TMPA** (weaker O–O and Cu–O bonds, slightly stronger Fe–O bond) is attributable to a combination of electronic and structural effects.

The DFT calculations provide particularly valuable insights into the impact of H-bonding to the O_2 π^*_v *versus* the O_2 π^*_σ orbital with respect to O–O cleavage chemistry. As has been previously shown,[27] O–O cleavage involves electron transfer from the Fe d_{yz} orbital into the O_2 σ* (which have π-symmetry overlap) and formation of a $Fe^{IV}{=}O$ product. The optimized structures (shown in Fig. 11A and B) reveal that binding *via* the O_2 π^*_v results in a longer O–O bond and shorter Fe–O bond than O_2 π^*_σ binding, suggesting weaker and stronger bonds, respectively. Additionally, H-bonding to O_2 π^*_v lowers the energy of the O_2 σ* orbital to a greater extent than H-bonding to O_2 π^*_σ, resulting in a smaller energy gap between the O_2 σ* and Fe d_{yz} orbital. *Applying these trends to O–O cleavage chemistry, which involves formation of a $Fe^{IV}{=}O$ product, these results suggest that H-bonding to the O_{Cu} atom via the O_2 π^*_v orbital (see Fig. 11B) gives the most effective orientation for activating O–O cleavage.*

Geometry optimizations of **LS-$^{(NH2)2}$TMPA** yielded two possible structures (energetic minima) differing in H-bond orientation, one with 2 H-bonds to O_{Cu} (with N(H)···O_{Cu} distances of 2.80 and 2.83 Å and ∠O_{Cu}HN of 156.6 and 161.0°), and the other comprising of 1 H-bond to O_{Cu} and 1 H-bond to O_{Fe} (with an N(H)$\cdots O_{Cu}$ distance of 2.84 Å, a $\angle O_{Cu}HN$ of 162.4°, an N(H)$\cdots O_{Fe}$ distance of 2.76 Å and a $\angle O_{Fe}HN$ of 168.4°; Fig. 10C, D and Table S2†). These were found to be very similar in energy (with the former being ~1 kcal mol^{-1} lower); a structure with two H-bonds to O_{Fe} was sufficiently higher in energy, such that one H-bond consistently reoriented to bind O_{Cu} upon unconstrained optimization. Comparing the O_{Cu},O_{Cu} and O_{Cu},O_{Fe} H-bonded structures, the former exhibits a weaker Cu–O bond and stronger Fe–O bond (as expected), as well as a weaker O–O bond. Relative to **LS-^{NH2}TMPA**, both structures agree with the observed trends in the rR data (O–O, Fe–O, and Cu–O bonds all weaken, but by different magnitudes). However, comparing the rR data on **LS-$^{(NH2)2}$TMPA** to **LS-^{NH2,CH3}TMPA** suggests that replacing the methyl group in the latter with an amine results in slightly weaker O–O, stronger Fe–O, weaker Cu–O bonds, based on the differences in stretching frequencies (Table 1). Considering the findings for **LS-^{NH2}TMPA**, these vibrational effects implicate H-bonding to the O_{Cu} atom (since binding O_{Fe} would be expected to weaken the Fe–O bond). Nevertheless, it is interesting that while incorporating one $-NH_2$ group (as in **LS-^{NH2}TMPA**) weakens the O–O bond and minimally affects the M–O bonds (even strengthening the Fe–O), addition of the second $-NH_2$ group acts to weaken all three core modes (based on the rR data, Table 1).

From the rR data above, minor increases in sterics ($-CH_3$ substitution) cause a decrease in the O–O, Fe–O, and Cu–O vibrations (Table 1), indicating that the bonds weaken and elongate. This behavior can be replicated computationally by constraining and systematically elongating the Fe$\cdots$Cu distance in **LS-TMPA**, which results in weakening of all three core modes, therefore suggesting that the steric consequence of the methyl group in ^{CH3}TMPA is to push the Fe and Cu moieties apart.

However, incorporating substituents with greater steric contributions, as in the amido-based groups of ^{PV}TMPA and ^{A2}TMPA, resulted in a different behavior of the core vibrational frequencies. As shown above, these bulkier ligands yielded very low frequency M–O stretches and high frequency O–O stretches, suggesting weak M–O bonds and strong O–O bonds. The DFT-optimized structure of **LS-^{PV}TMPA** exhibits an exceptionally small Fe–O–O–Cu dihedral angle (100°), a wide Fe–O–O angle (119°), and a seemingly weak H-bonding interaction to the O_{Cu} atom of the peroxo (O$\cdots$N(H) = 2.90 Å; the $\angle O_{Cu}HN = 164.4°$) *via* the $O_2^{\ 2-}\ \pi^*_\sigma$ orbital (Fig. 12A). In contrast, **LS-^{NH2}TMPA** showed a wider Fe–O–O–Cu dihedral angle (152°), smaller Fe–O–O angle (115°) and a stronger H-bond (O$\cdots$N(H) = 2.72 Å, *vide supra*) *via* the $O_2^{\ 2-}\ \pi^*_v$ orbital.

In agreement with the observed vibrational frequencies, the optimized **LS-^{PV}TMPA** structure exhibits relatively long M–O bonds and a short O–O bond (Table S5†), which would suggest low ν(M–O) and high ν(O–O) stretches (according to Badger's rule). Furthermore, a wider Fe–O–O angle (as in **LS-^{PV}TMPA**) would increase vibrational coupling of the Fe–O and O–O modes, resulting in even lower ν(Fe–O) and higher ν(O–O) frequencies. Interestingly, the optimized structure of **LS-^{A2}TMPA** (Fig. 12B) exhibits a shorter O$\cdots$N(H) distance (2.73 Å), but very similar core structure (with slightly shorter M–O and O–O bond lengths compared to **LS-^{PV}TMPA**, in excellent agreement with the trend in vibrational frequencies from the rR data), suggesting that the H-bond in these amido complexes has a minor impact on the core bond strengths. Offering insight into the intense low-energy band observed by UV-Vis for **LS-^{PV}TMPA** and **LS-^{A2}TMPA** (*vide supra*), the calculations also show that H-bonding to the $O_2\ \pi^*_\sigma$ orbital polarizes the $O_2\ \pi^*_v$ orbital toward the O_{Fe} atom, which would result in a more intense LMCT band. Taken together, these results suggest that the effect of H-bonding to the peroxo core in the amido-appended complexes differs from the amino-appended complexes by a combination of structural and electronic aspects.

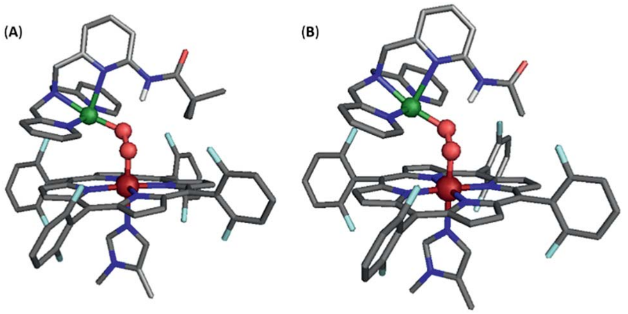

Fig. 12 Optimized structure for (A) LS-^{PV}TMPA and (B) LS-^{A2}TMPA. Note that the Cu geometry is now skewed toward square pyramidal (τ_5 = 0.22 and 0.16 for (A) and (B), respectively), unlike the optimized structures for LS-^{NH2}TMPA (Fig. S11†). Further, note the distorted dihedral angle of 100° and 107° (for (A) and (B), respectively) *vs.* 141° for LS-TMPA (Fig. S13A†).

Conclusions

Hydrogen bonding is prevalent in biology, especially concerning dioxygen chemistry in metalloenzymes (*i.e.*, globins, peroxidases, catalases, cytochrome P450's, oxidases).[6] The effects of intramolecular H-bonding will allow for interesting mechanistic studies for reductive O_2 cleavage; this could be invaluable in the design of more efficient fuel cells in which O_2 reduction is the key reaction occurring at the cathode. This study has fully characterized eight novel synthetic low-spin heme–peroxo–copper models inspired by cytochrome *c* oxidase active site chemistry; overall 16 complexes have been newly synthesized, which more than doubles reported analogous complexes in the literature.

The present work demonstrates the flexibility to design and synthesize various novel TMPA-based ligands and observe a range of effects (elucidated here), reinforcing the importance of a careful balance between sterics and hydrogen bonding being critical in enzyme active site reactions, those requiring specific H-bonding or protonation situations. This is especially shown using the ligands containing appended amido moieties, which have been shown to be strong H-bonding groups in previous studies (with copper-only complexes) but herein perturb the heme–peroxo–copper complex geometry, hindering significant H-bonding to the peroxo core.

The effects of intramolecular H-bonding on the heme–peroxo–Cu core were examined by UV-vis and rR spectroscopies and DFT calculations. It is shown that the H-bonding moieties (–NH_2, –$(NH_2)_2$, and –NH_2,CH_3) reproduce experimental data for intermolecular H-bonding effects reported for a related heme–peroxo–copper systems, and preferentially interact with the O_{Cu} atom of the peroxo; these findings offer a critical correlation to studies showing that an H-bonding interaction can lower the O–O cleavage barrier.[26,27] Importantly, while the nature of the H-bonding interaction could not be well understood in past studies due to complications including poorly defined Cu ligation and entropic costs, the ligand system employed herein provides a well-defined platform that is reliably modelled by computational means. This has delivered critical insight into an orientational anisotropy in H-bond activating the O–O bond for cleavage. Furthermore, while the metal–oxygen bond vibrations (especially Cu–O) are not observed for most synthetic heme–peroxo–copper species, these low-spin complexes for the first time allowed direct insight into the Cu–O bond; this is a paramount step towards future development of a more biomimetic, efficient model of C*c*O (with full access to modifications of new ligand systems and a deeper understanding of what is occurring during O_2 reduction studies). Overall, systematic control over H-bonding ability of the ^{X}TMPA ligands provides a foundation to draw conclusions about the effects of H-bonding on the thermodynamic stability, electronic structure, and reactivity of corresponding heme–peroxo–copper complexes.

Conflicts of interest

There are no conflicts to declare.

Acknowledgements

The research support of the U.S. National Institutes of Health (GM60353 to K. D. K., DK031450 to E. I. S.) is gratefully acknowledged.

Notes and references

§ See ESI† for more details.

¶ It should be noted that enhancement of all three core vibrational modes simultaneously (*e.g.*, with 413 nm excitation) may indicate significant coupling between these modes, and that this coupling can contribute to the observed vibrational frequencies (in addition to the bond strength).[79] However, the relative enhancement of the Fe–O/O–O/Cu–O modes at 413 nm excitation remains similar across these LS complexes (except the bulkier derivatives noted in the text), and it is therefore unlikely that the amount of coupling varies drastically.

‖ Adapted from ref. 36, but re-optimized here.

1 R. L. Shook and A. S. Borovik, *Inorg. Chem.*, 2010, **49**, 3646–3660.
2 S. A. Cook and A. S. Borovik, *Acc. Chem. Res.*, 2015, **48**, 2407–2414.
3 S. A. Cook, E. A. Hill and A. S. Borovik, *Biochemistry*, 2015, **54**, 4167–4180.
4 A. S. Borovik, *Acc. Chem. Res.*, 2005, **38**, 54–61.
5 S. M. Adam, G. B. Wijeratne, P. J. Rogler, D. E. Diaz, D. A. Quist, J. J. Liu and K. D. Karlin, *Chem. Rev.*, 2018, **118**, 10840–11022.
6 X. Huang and J. T. Groves, *Chem. Rev.*, 2018, **118**, 2491–2553.
7 M. Alfonso-Prieto, X. Biarnés, P. Vidossich and C. Rovira, *J. Am. Chem. Soc.*, 2009, **131**, 11751–11761.
8 M. Wikström, K. Krab and V. Sharma, *Chem. Rev.*, 2018, **118**, 2469–2490.
9 S. Yoshikawa and A. Shimada, *Chem. Rev.*, 2015, **115**, 1936–1989.
10 D. A. Quist, D. E. Diaz, J. J. Liu and K. D. Karlin, *J. Biol. Inorg Chem.*, 2017, **22**, 253–288.
11 E. I. Solomon, D. E. Heppner, E. M. Johnston, J. W. Ginsbach, J. Cirera, M. Qayyum, M. T. Kieber-Emmons, C. H. Kjaergaard, R. G. Hadt and L. Tian, *Chem. Rev.*, 2014, **114**, 3659–3853.
12 M. R. A. Blomberg, *Biochemistry*, 2016, **55**, 489–500.
13 M. Aki, T. Ogura, Y. Naruta, T. H. Le, T. Sato and T. Kitagawa, *J. Phys. Chem. A*, 2002, **106**, 3436–3444.
14 K. M. McCauley, J. M. Vrtis, J. Dupont and W. A. van der Donk, *J. Am. Chem. Soc.*, 2000, **122**, 2403–2404.
15 D. A. Pratt, R. P. Pesavento and W. A. van der Donk, *Org. Lett.*, 2005, **7**, 2735–2738.
16 L. Qin, J. Liu, D. A. Mills, D. A. Proshlyakov, C. Hiser and S. Ferguson-Miller, *Biochemistry*, 2009, **48**, 5121–5130.
17 I. D. Petrik, R. Davydov, M. Ross, X. Zhao, B. Hoffman and Y. Lu, *J. Am. Chem. Soc.*, 2016, **138**, 1134–1137.
18 M. R. A. Blomberg, P. E. M. Siegbahn and M. Wikström, *Inorg. Chem.*, 2003, **42**, 5231–5243.
19 B. Ravikiran and R. Mahalakshmi, *RSC Adv.*, 2014, **4**, 33958–33974.
20 L. Noodleman, W. G. Han Du, J. A. Fee, A. W. Götz and R. C. Walker, *Inorg. Chem.*, 2014, **53**, 6458–6472.
21 S. Yoshikawa, K. Muramoto and K. Shinzawa-Itoh, *Biochim. Biophys. Acta, Bioenerg.*, 2011, **1807**, 1279–1286.
22 S. Yoshikawa, K. Muramoto, K. Shinzawa-Itoh and M. Mochizuki, *Biochim. Biophys. Acta, Bioenerg.*, 2012, **1817**, 579–589.
23 N. Dominelli-Whiteley, J. J. Brown, K. B. Muchowska, I. K. Mati, C. Adam, T. A. Hubbard, A. Elmi, A. J. Brown, I. A. W. Bell and S. L. Cockroft, *Angew. Chem., Int. Ed.*, 2017, **56**, 7658–7662.
24 V. Sharma and M. Wikström, *Biochim. Biophys. Acta, Bioenerg.*, 2016, **1857**, 1111–1115.
25 K. Muramoto, K. Ohta, K. Shinzawa-Itoh, K. Kanda, M. Taniguchi, H. Nabekura, E. Yamashita, T. Tsukihara and S. Yoshikawa, *Proc. Natl. Acad. Sci.*, 2010, **107**, 7740–7745.
26 S. M. Adam, I. Garcia-Bosch, A. W. Schaefer, S. K. Sharma, M. A. Siegler, E. I. Solomon and K. D. Karlin, *J. Am. Chem. Soc.*, 2017, **139**, 472–481.
27 A. W. Schaefer, M. T. Kieber-Emmons, S. M. Adam, K. D. Karlin and E. I. Solomon, *J. Am. Chem. Soc.*, 2017, **139**, 7958–7973.
28 M. R. A. Blomberg and P. E. R. E. M. Siegbahn, *J. Comput. Chem.*, 2006, **27**, 1373–1384.
29 M. R. A. Blomberg, T. Borowski, F. Himo, R.-Z. Liao and P. E. M. Siegbahn, *Chem. Rev.*, 2014, **114**, 3601–3658.

30 F. Poiana, C. Von Ballmoos, N. Gonska, M. R. A. Blomberg, P. Ädelroth and P. Brzezinski, *Sci. Adv.*, 2017, **3**, e1700279.

31 Z. Halime, M. T. Kieber-Emmons, M. F. Qayyum, B. Mondal, T. Gandhi, S. C. Puiu, E. E. Chufán, A. A. N. Sarjeant, K. O. Hodgson, B. Hedman, E. I. Solomon and K. D. Karlin, *Inorg. Chem.*, 2010, **49**, 3629–3645.

32 S. Fukuzumi, H. Kotani, H. R. Lucas, K. Doi, T. Suenobu, R. L. Peterson and K. D. Karlin, *J. Am. Chem. Soc.*, 2010, **132**, 6874–6875.

33 R. A. Ghiladi, E. E. Chufán, D. del Río, E. I. Solomon, C. Krebs, B. H. Huynh, H.-W. Huang, P. Moënne-Loccoz, S. Kaderli, M. Honecker, A. D. Zuberbühler, L. Marzilli, R. J. Cotter and K. D. Karlin, *Inorg. Chem.*, 2007, **46**, 3889–3902.

34 K. D. Karlin, A. Nanthakumar, S. Fox, N. N. Murthy, N. Ravi, B. H. Huynh, R. D. Orosz and E. P. Day, *J. Am. Chem. Soc.*, 1994, **116**, 4753–4763.

35 S. Hematian, I. Garcia-Bosch and K. D. Karlin, *Acc. Chem. Res.*, 2015, **48**, 2462–2474.

36 I. Garcia-Bosch, S. M. Adam, A. W. Schaefer, S. K. Sharma, R. L. Peterson, E. I. Solomon and K. D. Karlin, *J. Am. Chem. Soc.*, 2015, **137**, 1032–1035.

37 D. del Río, R. Sarangi, E. E. Chufán, K. D. Karlin, B. Hedman, K. O. Hodgson and E. I. Solomon, *J. Am. Chem. Soc.*, 2005, **127**, 11969–11978.

38 Z. Halime, H. Kotani, Y. Li, S. Fukuzumi and K. D. Karlin, *Proc. Natl. Acad. Sci. U. S. A.*, 2011, **108**, 13990–13994.

39 R. A. Ghiladi, T. D. Ju, D. H. Lee, P. Moënne-Loccoz, S. Kaderli, Y. M. Neuhold, A. D. Zuberbühler, A. S. Woods, R. J. Cotter and K. D. Karlin, *J. Am. Chem. Soc.*, 1999, **121**, 9885–9886.

40 R. A. Ghiladi, K. R. Hatwell, K. D. Karlin, H. Huang, P. Moënne-Loccoz, C. Krebs, B. H. Huynh, L. A. Marzilli, R. J. Cotter, S. Kaderli and A. D. Zuberbühler, *J. Am. Chem. Soc.*, 2001, **123**, 6183–6184.

41 M.-A. Kopf, Y.-M. Neuhold, A. D. Zuberbühler and K. D. Karlin, *Inorg. Chem.*, 1999, **38**, 3093–3102.

42 H. V. Obias, G. P. F. Van Strijdonck, D. H. Lee, M. Ralle, N. J. Blackburn and K. D. Karlin, *J. Am. Chem. Soc.*, 1998, **120**, 9696–9697.

43 S. Fox, A. Nanthakumar, M. Wikström, K. D. Karlin and N. J. Blackburn, *J. Am. Chem. Soc.*, 1996, **118**, 24–34.

44 J. C. M. Rivas, S. L. Hinchley, L. Metteau and S. Parsons, *Dalton Trans.*, 2006, 2316.

45 T. Sasaki, N. Nakamura and Y. Naruta, *Chem. Lett.*, 1998, **27**, 351.

46 Y. Naruta, T. Sasaki, F. Tani, Y. Tachi, N. Kawato and N. Nakamura, *J. Inorg. Biochem.*, 2001, **83**, 239–246.

47 J. G. Liu, Y. Naruta and F. Tani, *Chem.–Eur. J.*, 2007, **13**, 6365–6378.

48 J. P. Collman, P. C. Herrmann, B. Boitrel, X. Zhang, T. A. Eberspacher, L. Fu, J. Wang, D. L. Rousseau and E. R. Williams, *J. Am. Chem. Soc.*, 1994, **116**, 9783–9784.

49 S. Yamaguchi, A. Wada, Y. Funahashi, S. Nagatomo, T. Kitagawa, K. Jitsukawa and H. Masuda, *Eur. J. Inorg. Chem.*, 2003, **2003**, 4378–4386.

50 A. Wada, Y. Honda, S. Yamaguchi, S. Nagatomo, T. Kitagawa, K. Jitsukawa and H. Masuda, *Inorg. Chem.*, 2004, **43**, 5725–5735.

51 M. Bhadra, J. Y. C. Lee, R. E. Cowley, S. Kim, M. A. Siegler, E. I. Solomon and K. D. Karlin, *J. Am. Chem. Soc.*, 2018, **140**, 9042–9045.

52 R. A. Ghiladi, K. R. Hatwell, K. D. Karlin, H.-W. Huang, P. Moënne-Loccoz, C. Krebs, L. A. Marzilli, R. J. Cotter, S. Kaderli and A. D. Zuberbühler, *J. Am. Chem. Soc.*, 2001, **123**, 6183–6184.

53 E. Kim, M. E. Helton, I. M. Wasser, K. D. Karlin, S. Lu, H.-W. Huang, P. Moenne-Loccoz, C. D. Incarvito, A. L. Rheingold, M. Honecker, S. Kaderli and A. D. Zuberbuhler, *Proc. Natl. Acad. Sci. U. S. A.*, 2003, **100**, 3623–3628.

54 E. Kim, E. E. Chufán, K. Kamaraj and K. D. Karlin, *Chem. Rev.*, 2004, **104**, 1077–1134.

55 E. E. Chufán, B. Mondal, T. Gandhi, E. Kim, N. D. Rubie, P. Moënne-Loccoz and K. D. Karlin, *Inorg. Chem.*, 2007, **46**, 6382–6394.

56 Z. Halime, M. T. Kieber-Emmons, M. F. Qayyum, B. Mondal, T. Gandhi, S. C. Puiu, E. E. Chufán, A. A. N. Sarjeant, K. O. Hodgson, B. Hedman, E. I. Solomon and K. D. Karlin, *Inorg. Chem.*, 2010, **49**, 3629–3645.

57 D. del Río, R. Sarangi, E. E. Chufán, K. D. Karlin, B. Hedman, K. O. Hodgson and E. I. Solomon, *J. Am. Chem. Soc.*, 2005, **127**, 11969–11978.

58 T. Chishiro, Y. Shimazaki, F. Tani, Y. Tachi, Y. Naruta, S. Karasawa, S. Hayami and Y. Maeda, *Angew. Chem., Int. Ed.*, 2003, **42**, 2788–2791.

59 R. A. Ghiladi, R. M. Kretzer, I. Guzei, A. L. Rheingold, Y.-M. Neuhold, K. R. Hatwell, A. D. Zuberbühler and K. D. Karlin, *Inorg. Chem.*, 2001, **40**, 5754–5767.

60 T. D. Ju, R. A. Ghiladi, D.-H. Lee, G. P. F. van Strijdonck, A. S. Woods, R. J. Cotter, V. G. Young and K. D. Karlin, *Inorg. Chem.*, 1999, **38**, 2244–2245.

61 P. S. Braterman, R. C. Davies and R. J. P. Williams, *Adv. Chem. Phys.*, 1964, **7**, 359–407.

62 E. Kim, E. E. Chufán, K. Kamaraj and K. D. Karlin, *Chem. Rev.*, 2004, **104**, 1077–1133.

63 M. T. Kieber-Emmons, Y. Li, Z. Halime, K. D. Karlin and E. I. Solomon, *Inorg. Chem.*, 2011, **50**, 11777–11786.

64 D. K. Dogutan, S. A. Stoian, R. McGuire, M. Schwalbe, T. S. Teets and D. G. Nocera, *J. Am. Chem. Soc.*, 2011, **133**, 131–140.

65 S. Chatterjee, K. Sengupta, B. Mondal, S. Dey and A. Dey, *Acc. Chem. Res.*, 2017, **50**, 1744–1753.

66 K. Mittra, K. Sengupta, A. Singha, S. Bandyopadhyay, S. Chatterjee, A. Rana, S. Samanta and A. Dey, *J. Inorg. Biochem.*, 2016, **155**, 82–91.

67 K. Mittra, S. Chatterjee, S. Samanta, K. Sengupta, H. Bhattacharjee and A. Dey, *Chem. Commun.*, 2012, **48**, 10535–10537.

68 M. Gregory, P. J. Mak, S. G. Sligar and J. R. Kincaid, *Angew. Chem., Int. Ed.*, 2013, **52**, 5342–5345.

69 P. J. Mak, W. Thammawichai, D. Wiedenhoeft and J. R. Kincaid, *J. Am. Chem. Soc.*, 2015, **137**, 349–361.

70 E. Kim, K. Kamaraj, B. Galliker, N. D. Rubie, P. Moënne-Loccoz, S. Kaderli, A. D. Zuberbühler and K. D. Karlin, *Inorg. Chem.*, 2005, **44**, 1238–1247.

71 E. Kim, J. Shearer, S. Lu, P. Moenne-Loccoz, M. E. Helton, S. Kaderli, A. D. Zuberbuhler and K. D. Karlin, *J. Am. Chem. Soc.*, 2004, **126**, 12716–12717.

72 J.-G. Liu, Y. Naruta and F. Tani, *Chem.–Eur. J.*, 2007, **13**, 6365–6378.

73 J. P. Collman, C. J. Sunderland, K. E. Berg, M. A. Vance and E. I. Solomon, *J. Am. Chem. Soc.*, 2003, **125**, 6648–6649.

74 J.-G. Liu, Y. Naruta and F. Tani, *Angew. Chem., Int. Ed.*, 2005, **44**, 1836–1840.

75 J. Liu, Y. Naruta, F. Tani, T. Chishiro and Y. Tachi, *Chem. Commun.*, 2004, 120–121.

76 V. Sharma, M. Wikström and V. R. I. Kaila, *Biochim. Biophys. Acta, Bioenerg.*, 2011, **1807**, 813–818.

77 Y. Yoshioka, H. Kawai and K. Yamaguchi, *Chem. Phys. Lett.*, 2003, **374**, 45–52.

78 R. L. Peterson, R. A. Himes, H. Kotani, T. Suenobu, L. Tian, M. A. Siegler, E. I. Solomon, S. Fukuzumi and K. D. Karlin, *J. Am. Chem. Soc.*, 2011, **133**, 1702–1705.

79 K. Bajdor, J. R. Kincaid and K. Nakamoto, *J. Am. Chem. Soc.*, 1984, **106**, 7741–7747.